Ocean Engineering 312 (2024) 119241

Contents lists available at ScienceDirect

Ocean Engineering

journal homepage: www.elsevier.com/locate/oceaneng

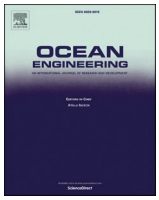

Research paper

Peridynamic modelling of elastic and viscoelastic behaviour in polycrystalline ice: A study using NOSBPD and PDCHT

Yakubu Kasimu Galadima [a,b], Erkan Oterkus [a,*], Selda Oterkus [a]

[a] PeriDynamics Research Centre, Department of Naval Architecture, Ocean and Marine Engineering, University of Strathclyde, Glasgow, United Kingdom
[b] Department of Civil Engineering, Ahmadu Bello University, Zaria, Nigeria

ARTICLE INFO

Keywords:
Peridynamics
Homogenization
Polycrystalline ice
Isotropy
Effective properties

ABSTRACT

This study explores the elastic and viscoelastic behaviour of ice using the Non-Ordinary State-Based Peridynamic (NOSBPD) framework. A primary objective is to extend and validate the applicability of NOSBPD in modelling the complex responses of ice under various conditions. The study employs the Peridynamic Computational Homogenization Theory (PDCHT) to determine the critical threshold of grain count necessary to induce an effectively isotropic response in polycrystalline S2 ice. Results are consistent with previous findings from Finite Element Method (FEM) and Bond-Based Peridynamics (BBPD) studies.

Furthermore, the viscoelastic response of ice is investigated by integrating a viscoelastic constitutive model into the NOSBPD framework. A benchmark problem of a viscoelastic ice sample subjected to tensile stress is simulated, with results compared against FEM simulations conducted in ANSYS Mechanical. The findings show good agreement, validating the NOSBPD framework's capability to capture time-dependent viscoelastic behaviour of ice accurately.

The study contributes to the field of ice mechanics by demonstrating the robustness and versatility of NOSBPD in modelling both elastic and viscoelastic responses of ice. These advancements enhance the credibility and applicability of peridynamics (PD) as a powerful tool for simulating complex material behaviours, paving the way for further research and practical applications in ice engineering.

1. Introduction

The study of the mechanics of ice is crucial for a wide range of engineering and environmental applications. Understanding the mechanical behaviour of ice is essential for designing and maintaining structures in cold regions, such as icebreakers, offshore platforms, and bridges. Additionally, it is vital for predicting the impact of climate change on polar ice masses and sea levels. Traditional methods of analysing ice behaviour have predominantly relied on classical continuum mechanics (CCM). While CCM is well-established, it often faces challenges in modelling complex phenomena, such as simulating discontinuous damage mechanisms like the formation and propagation of cracks, and damage mechanisms like strain-softening due to distributed microcracking.

One of the primary limitations of CCM is that the partial derivatives characterizing its field equations break down in the face of discontinuous material responses such as fractures. However, the nucleation and accumulation of microcracks is known to significantly impact the response of ice, which can be nonlinear, elastic, or viscoelastic depending on the loading condition (Duddu et al., 2013). Any candidate theory of mechanics that seeks to be successful in modelling ice and its complex response will have to be able to circumvent the limitations of the CCM.

Peridynamics (PD), introduced in (Silling, 2000) as a reformulation of CCM, offers significant advantages in addressing these limitations. Unlike CCM, which relies on local differential equations, PD employs integral equations that remain well-defined even in the presence of discontinuities like cracks. This nonlocal approach makes PD particularly suitable for simulating fracture and other complex behaviours that are difficult to handle with methods based on the CCM.

PD circumvents the mathematical limitations of classical theory by replacing the spatial derivatives in the equations of motion with integral operators. Consequently, PD does not require a continuously differentiable displacement field. Evolving discontinuities, such as crack initiation and propagation, are treated as inherent characteristics of the material and are modelled using the fundamental PD equations of

* Corresponding author.
E-mail address: erkan.oterkus@strath.ac.uk (E. Oterkus).

https://doi.org/10.1016/j.oceaneng.2024.119241
Received 13 October 2023; Received in revised form 9 September 2024; Accepted 9 September 2024
Available online 12 September 2024

motion without additional assumptions or modifications. This advantage has spurred growing interest in using PD to characterize materials with strong or evolving discontinuous responses (Galadima et al., 2022; Candaş et al., 2020). Previous research has demonstrated the potential of PD in capturing the complex responses of various materials under different loading conditions (Galadima et al., 2023a; Gu et al., 2019).

Building upon these insights, peridynamics is increasingly utilized to characterize the complex behaviour of ice. A comprehensive survey of existing literature reveals a growing body of research dedicated to harnessing the power of peridynamics to study the response of ice. This expanding exploration encompasses various peridynamic theories—BBPD, Ordinary State-Based Peridynamics (OSBPD), and NOSBPD—each contributing uniquely to the growing understanding of ice behaviour.

Within the framework of BBPD, studies have successfully modelled inhomogeneous ice, incorporating inhomogeneity via a Weibull-distributed critical bond stretch to conduct thermomechanical field analysis of crack propagation (Song et al., 2023). Another study employed a BBPD approach to develop a model for the fracture behaviour of polycrystalline ice under dynamic loading conditions, demonstrating the method's capability to simulate the fracture accurately and compare it favourably with finite element analysis (Lu et al., 2020). Additionally, the coupling of BBPD with Updated Lagrangian Particle Hydrodynamics (ULPH) has been explored to simulate the interaction between ice and seawater, effectively capturing the dynamics of ice-breaking processes (Liu et al., 2020).

The application of OSBPD has also gained traction in ice mechanics. For instance, OSBPD has been utilized to investigate the numerical modelling of columnar polycrystalline ice, determining the minimum number of grains required to maintain isotropy and accurately characterizing polycrystalline materials (Li et al., 2023).

The NOSBPD has been employed to model the impact-induced fragmentation of ice using a viscoelastic-plastic material model integrated with the Drucker-Prager constitutive model (Song et al., 2018). Furthermore, a study on ice crater formation due to impact loads implemented adaptive particle refinement within the NOSBPD framework, demonstrating the method's predictive capacity and efficiency (Song et al., 2019). Additionally, NOSBPD has been used to simulate the interaction between level ice and a cylindrical rigid structure, showing good agreement with experimental data and highlighting its applicability in modelling complex ice-structure interactions (Liu et al., 2017).

The primary objective of this study is to explore the elastic and viscoelastic behaviour of ice using the NOSBPD framework. By validating NOSBPD through benchmark problems, this research aims to contribute to the expanding discourse on the applicability of PD by demonstrating its effectiveness and robustness in ice mechanics. This will be achieved by employing NOSBPD to simulate the response of ice in both elastic and viscoelastic regimes.

In the elastic regime, this study will employ PDCHT to determine the critical threshold of grain count necessary to induce an effectively isotropic response in polycrystalline S2 ice. In the viscoelastic regime, a convolution-type viscoelastic constitutive model based on CCM will be adapted and implemented within the NOSBPD to investigate the viscoelastic response of ice.

The aim of this study is to contribute to the ongoing effort of validating PD as an effective mathematical modelling tool, thereby enhancing its credibility and applicability in the field of ice mechanics. The manuscript is structured as follows: Section 2.0 outlines the theoretical framework of peridynamics, focusing on the NOSBPD. Section 3.0 discusses CCM constitutive models to be incorporated into the NOSBPD framework in this study, detailing both the elastic and viscoelastic regimes.

Section 4.0 presents an overview of PDCHT. Section 5.0 presents the validation of NOSBPD using PDCHT to determine the critical grain count for isotropy in polycrystalline S2 ice. Section 6.0 examines the viscoelastic response of ice through NOSBPD simulations, including the implementation of constitutive models and benchmark problem analyses. Finally, Section 7.0 concludes the study by summarizing key findings, contributions, and potential directions for further research.

2. Theoretical framework

In PD, the state of a material point $\boldsymbol{x}$ in a body $\mathscr{B}$ is determined by the net effect of its interaction with all points located within a finite distance. The interaction between a primary point $\boldsymbol{x}$, which is a point under consideration, and a secondary point $\boldsymbol{x}'$ is called a *bond*. The distance $\boldsymbol{\xi}_{\boldsymbol{x}} = \boldsymbol{x}' - \boldsymbol{x}$ in the undeformed configuration between $\boldsymbol{x}$ and $\boldsymbol{x}'$ is called *bond length* or a 'bond' for short. The intended meaning of the term 'bond' when used is usually discerned from the context. The maximum distance, denoted as δ, over which a primary point is allowed to interact with other points is called its horizon. The region defined by δ for a primary point $\boldsymbol{x}$ is sometimes referred to as its domain of influence, such that the set:

$$\mathscr{B}_{\delta}(\boldsymbol{x}) = \{\boldsymbol{x}' \in \mathscr{R} : |\boldsymbol{x}' - \boldsymbol{x}| < \delta\} \tag{1}$$

containing points $\boldsymbol{x}'$ interacting with $\boldsymbol{x}$ is called its family. Also, the set

$$\mathscr{K} = \{\boldsymbol{\xi}_{\boldsymbol{x}} \in (\mathbb{R}\backslash\mathbf{0}) | (\boldsymbol{\xi}_{\boldsymbol{x}} + \boldsymbol{x}) \in (\mathscr{B}_{\delta}(\boldsymbol{x}) \cap \mathscr{B})\} \tag{2}$$

is the family of bonds for $\boldsymbol{x}$. The equation that tracks the motion of a primary point $\boldsymbol{x}$ at time t in the SBPD framework is given by the field equation:

$$\rho(\boldsymbol{x})\ddot{\boldsymbol{u}}(\boldsymbol{x},t) = \int_{\mathscr{H}_{\boldsymbol{x}}} \{\underline{\mathbf{T}}[\boldsymbol{x},t]\langle \boldsymbol{x}' - \boldsymbol{x}\rangle - \underline{\mathbf{T}}[\boldsymbol{x}',t]\langle \boldsymbol{x} - \boldsymbol{x}'\rangle dV_{\boldsymbol{x}'} + \mathbf{b}(\boldsymbol{x},t) \tag{3}$$

where $\boldsymbol{u}$ and $\mathbf{b}$ represents displacement and body force vectors, and $\underline{\mathbf{T}}$ is defined as a *vector force state*. The notion of *PD states* or *states* for short is a central feature of SBPD that distinguishes it from the BBPD framework. Within this framework, a state constitutes a mathematical function that is defined on bonds so that for a primary point $\boldsymbol{x}$, the force state $\underline{\mathbf{T}}$ associate each element of (2) with some force density function $\mathbf{t}(\boldsymbol{x}, \boldsymbol{x}', t)$ that is vector-valued. The definition of the force state $\underline{\mathbf{T}}$ leads to the emergence of two distinct material models within the framework of SBPD. When $\underline{\mathbf{T}}$ is defined such that the force density function $\mathbf{t}(\boldsymbol{x}, \boldsymbol{x}', t)$ aligns with the corresponding bond $\boldsymbol{\xi}_{\boldsymbol{x}}$, it is termed an 'ordinary state,' resulting in the so-called OSBPD model, otherwise is termed a "non-ordinary state," giving rise to the NOSBPD model.

The NOSBPD model offers a more comprehensive modelling framework. In this communication, we will utilise a specific subclass of NOSBPD known as the "correspondence PD model." This model, in addition to the advantages it offers as a NOSBPD model, possesses the unique capability of accommodating constitutive models from the CCT. The force state $\underline{\mathbf{T}}$ in the correspondence model is defined such that:

$$\underline{\mathbf{T}}[\boldsymbol{x},t]\langle \boldsymbol{\xi}\rangle = \omega(|\boldsymbol{\xi}|)\mathbf{P}\mathbf{K}^{-1}\boldsymbol{\xi} \tag{4}$$

where ω is a scalar-valued weight function that quantifies the effect of the deformed bond $\boldsymbol{\xi}$ on the force field at the point $\boldsymbol{x}$. The specific form of the weight function used in this study is unity, (i.e. $\omega = 1$). The function $\mathbf{P} = \widehat{\mathbf{P}}(\mathbf{F})$ represents the first Piola-Kirchhoff stress tensor, which is derived from the material model $\widehat{\mathbf{P}}$ based on the classical theory as a function of the deformation gradient $\mathbf{F}$. The nonlocal deformation gradient is approximated (Silling et al., 2007) by the expression:

$$\mathbf{F}(\boldsymbol{x}) = \left[\int_{\mathscr{H}_{\boldsymbol{x}}} \underline{\omega}\langle \boldsymbol{\xi}\rangle (\boldsymbol{y}(\boldsymbol{x}',t) - \boldsymbol{y}(\boldsymbol{x},t)) \bigotimes \boldsymbol{\xi} d\boldsymbol{x}'\right]\mathbf{K}^{-1} \tag{5}$$

and $\mathbf{K}$ is a second order shape tensor defined to be:

$$\mathbf{K} = \int_{\mathscr{H}_{\boldsymbol{x}}} \underline{\omega}\langle \boldsymbol{\xi}\rangle \boldsymbol{\xi} \bigotimes \boldsymbol{\xi} dV_{\boldsymbol{\xi}} \tag{6}$$

The first Piola-Kirchhoff stress tensor and the Cauchy stress tensor

are related through the expression:

$$\mathbf{P} = J\boldsymbol{\sigma}\mathbf{F}^{-T}, J = det(\mathbf{F}) \tag{7}$$

If the assumption of small perturbation is made, then $\mathbf{F} \cong \mathbf{I}$, $J \cong 1$, and hence $\mathbf{P} = \boldsymbol{\sigma}$ in (7), and thus (4) can be written as:

$$\underline{\mathbf{T}}[\boldsymbol{x}, t]\langle\boldsymbol{\xi}\rangle = \omega(|\boldsymbol{\xi}|)\boldsymbol{\sigma}\mathbf{K}^{-1}\boldsymbol{\xi} \tag{8}$$

3. Elastic and viscoelastic constitutive models for ice

The NOSBPD offers the flexibility to incorporate a wide range of constitutive models from classical continuum mechanics (CCM). This allows the leveraging of the state-of-the-art of CCM and the advantages offered by PD in the analysis of complex material systems. In this section, the focus will be on introducing the constitutive models that underpin this study's analysis of ice, both in its elastic and viscoelastic regimes. In the elastic regime, the generalized Hooke's law will be utilized to describe the linear relationship between stress and strain in ice. This law will be extended to accommodate the transversely isotropic nature of ice.

Following the elastic model, a convolution-type integral viscoelastic constitutive model will be introduced to capture the time-dependent behaviour of ice. Viscoelasticity encompasses both the elastic and viscous characteristics of materials, making it essential for accurately modelling the long-term behaviour of ice under sustained loads. The integral form of the viscoelastic model allows for the incorporation of hereditary effects, providing a robust framework for understanding the creep and relaxation behaviours observed in ice.

3.1. Elasticity of ice

The elastic response of ice under stress is well-documented through various laboratory measurements. These measurements have indicated that ice can be assumed to respond elastically when the period of load application is less than 100 s for stress levels below 1 MN/m^2, or if the load to failure occurs within approximately 2 s (Gold, 1977). This elastic assumption simplifies the analysis and allows for the application of classical elastic theories to describe the mechanical behaviour of ice under certain conditions.

S2 columnar ice, characterized by its hexagonal crystal structure, exhibits unique mechanical properties that differ significantly from those of isotropic materials. The hexagonal structure of S2 ice necessitates the modelling of its elastic stiffness tensor as transversely isotropic. This means that the material possesses a single axis of symmetry, which leads to distinct mechanical properties along the axis of symmetry compared to those in the perpendicular directions. Utilizing the Voigt notation, the 3-D elastic stiffness tensor of the S2 columnar ice can be written as (Elvin, 1996):

$$\mathbf{C}^{3D} = \begin{bmatrix} C_{11}^{3D} & C_{12}^{3D} & C_{12}^{3D} & 0 & 0 & 0 \\ & C_{22}^{3D} & C_{13}^{3D} & 0 & 0 & 0 \\ & & C_{22}^{3D} & 0 & 0 & 0 \\ & & & 1/2(C_{22}^{3D} - C_{13}^{3D}) & 0 & 0 \\ & \text{Sym} & & & C_{55}^{3D} & 0 \\ & & & & & C_{55}^{3D} \end{bmatrix} \tag{9}$$

Given that the elastic behaviour of ice is recognized to be temperature-dependent, (Gammon et al., 1983) introduced an empirical relationship to calculate the elastic stiffness tensor (9) at temperature T, as outlined below:

$$\mathbf{C}^{3D}(T) = \mathbf{C}^{3D}(T_{\text{ref}}) \frac{(1 - 1.418 \times 10^{-3}T)}{(1 - 1.418 \times 10^{-3}T_{\text{ref}})} \tag{10}$$

where T_{ref} denotes the reference temperature at which the elastic stiffness tensor $\mathbf{C}^{3D}$ was determined. Based on (10), the Young's modulus E, was also shown to be temperature depended, and for a given temperature T, it can be obtained from

$$\mathrm{E}(T) = \mathrm{E}(T_{\text{ref}}) \frac{(1 - 1.418 \times 10^{-3}T)}{(1 - 1.418 \times 10^{-3}T_{\text{ref}})} \tag{11}$$

The Poisson's ratio was shown to be temperature independent. If we make the practical assumption that a plane stress condition applies, then the stiffness tensor (9) in two dimensions can be expressed as follows:

$$\mathbf{C}^{2D} = \begin{bmatrix} C_{11}^{2D} & C_{12}^{2D} & 0 \\ C_{12}^{2D} & C_{22}^{2D} & 0 \\ 0 & 0 & C_{33}^{2D} \end{bmatrix} \tag{12}$$

where the components C_{ij}^{2D} in (12) are obtained from the following relations (Elvin, 1996):

$$C_{11}^{2D} = C_{11}^{3D} - \frac{C_{13}^{3D}C_{31}^{3D}}{C_{33}^{3D}}, C_{12}^{2D} = C_{12}^{3D} - \frac{C_{13}^{3D}C_{32}^{3D}}{C_{33}^{3D}}, C_{21}^{2D} = C_{21}^{3D} - \frac{C_{23}^{3D}C_{31}^{3D}}{C_{33}^{3D}}$$
$$C_{22}^{2D} = C_{22}^{3D} - \frac{C_{23}^{3D}C_{32}^{3D}}{C_{33}^{3D}}, C_{33}^{2D} = C_{33}^{3D} \tag{13}$$

The material tensors (9) and (12) are defined in relation to the local axes of the crystal, as illustrated in Fig. 1. However, when representing the ice as a polycrystal, it becomes necessary to transform the components of the elastic tensor into a global axes system. In a two-dimensional scenario, the components of the fourth-order stiffness tensor (12) undergo transformation according to the following rule (Elvin, 1996):

$$\mathbf{C}_G = \boldsymbol{R}^T\mathbf{C}_L\boldsymbol{R} \tag{14}$$

In (14), the subscripts G and L respectively indicate global and local quantities, and R represents the transformation tensor, as expressed by:

$$\boldsymbol{R} = \begin{bmatrix} \cos^2(\zeta) & \sin^2(\zeta) & \frac{1}{2}\sin(2\zeta) \\ \sin^2(\zeta) & \cos^2(\zeta) & -\frac{1}{2}\sin(2\zeta) \\ -\sin(2\zeta) & \sin(2\zeta) & \cos(2\zeta) \end{bmatrix} \tag{15}$$

where ζ represents the angle between the c-axis of a crystal and the global x_1 axis.

3.2. Viscoelastic constitutive model for ice

Under a wide range of engineering conditions, polycrystalline ice

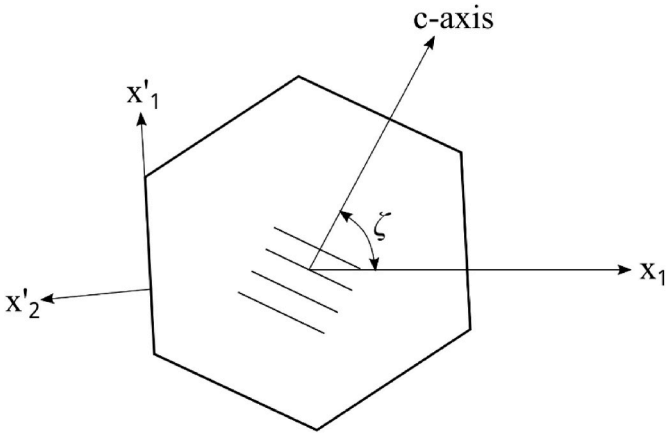

Fig. 1. Schematic representation of ice grain geometry.

exhibits characteristics of a brittle, viscoelastic material (Shi et al., 2017). This means that the material not only deforms elastically under stress but also undergoes time-dependent deformation, which is characteristic of viscoelastic materials. To incorporate this viscoelastic response in our study, the convolution-type integral viscoelastic constitutive model will be utilized. Specifically, this study will employ a formulation that uses the Prony series representation of the viscoelastic properties.

In this formulation, the constitutive equation governing the viscoelastic response can be written as:

$$\boldsymbol{\sigma}(t) = \boldsymbol{\sigma}_S + \boldsymbol{\sigma}_D = \int_0^t 3K(t-\tau)\frac{\partial \varepsilon_S(\tau)}{\partial \tau} d\boldsymbol{\varepsilon}_S(\tau) + \int_0^t 2G(t-\tau)\frac{\partial \boldsymbol{\varepsilon}_D(\tau)}{\partial \tau} d\boldsymbol{\varepsilon}_d(\tau) \tag{16}$$

where K and G are respectively the bulk and shear relaxation functions, $\boldsymbol{\sigma}$ and $\boldsymbol{\varepsilon}$ denote the stress and strain tensors respectively, and the subscripts S and D respectively denotes the spherical and deviatoric components of these tensors. The relaxation functions K and G can be expressed in terms of Prony series as:

$$K(t) = K_\infty + \sum_{i=1}^{n_K} K_i e^{-\left(t/\left(\tau_i^K\right)\right)}, G(t) = G_\infty + \sum_{i=1}^{n_G} G_i e^{-\left(t/\left(\tau_i^G\right)\right)} \tag{17}$$

Viscoelastic response in ice is known to be driven primarily by shear stress, while the volumetric change is governed by elasticity (Londono et al., 2016). Therefore, the general constitutive equation can be modified to account for this behaviour. In this regard, (16) is restated as follows:

$$\boldsymbol{\sigma}(t) = 3K\varepsilon_s \mathbb{I} + \int_0^t 2G(t-\tau)\frac{\partial \boldsymbol{\varepsilon}_D(\tau)}{\partial \tau} d\boldsymbol{\varepsilon}_d(\tau) \tag{18}$$

Such that $K(t) = K$ and $\mathbb{I}$ is identity tensor. From (17), the relationship between the extreme values of the shear modulus can be established as:

$$G(0) = G_\infty + \sum_{i=1}^{n_G} G_i \equiv G_0 \tag{19}$$

where: G_∞ is the shear relaxation modulus at equilibrium (that is after a long period of time), and G_0 is the glassy shear relaxation function (also referred to as the instantaneous shear relaxation modulus). Equation (19) leads to another form of the Prony series representation of the shear modulus as:

$$G(t) = G_0 - \sum_{i=1}^{n_G} G_i\left(1 - e^{-(t/(\tau_i))}\right) \tag{20}$$

Equation (18) is implemented within the NOSBPD framework alongside the Prony series representation of $G(t)$ given in (17) or (20).

3.3. Numerical implementation of viscoelastic model in NOSBPD

The viscoelastic constitutive model (18) is introduced into the NOSBPD field equation (3) via (8) to obtain:

$$\underline{\mathbf{T}}[\boldsymbol{x}, t]\langle \boldsymbol{\xi} \rangle = \omega(|\boldsymbol{\xi}|)\left[3K\varepsilon_s \mathbb{I} + \int_0^t 2G(t-\tau)\frac{\partial \boldsymbol{\varepsilon}_D(\tau)}{\partial \tau} d\boldsymbol{\varepsilon}_d(\tau)\right]\mathbf{K}^{-1}\boldsymbol{\xi} \tag{21}$$

If we substitute for the shear relaxation modulus in equation (21) with the Prony series expression in (20), we obtain:

$$\underline{\mathbf{T}}[\boldsymbol{x}, t]\langle \boldsymbol{\xi} \rangle = \omega(|\boldsymbol{\xi}|)\left[3K\varepsilon_s \mathbb{I} + 2G_0\left(\boldsymbol{\varepsilon}_D - \sum_{i=1}^{n_G} \alpha_i \boldsymbol{\varepsilon}_{Di}\right)\right]\mathbf{K}^{-1}\boldsymbol{\xi} \tag{22}$$

where

$$\alpha_i = \frac{G_i}{G_0}; \quad \boldsymbol{\varepsilon}_{Di} = \int_0^t \left(1 - e^{-((t-\tau)/(\tau_i))}\right)\frac{d\boldsymbol{\varepsilon}_D(\tau)}{d\tau} d\tau \tag{23}$$

In (23), α_i is the relative modulus of term i, and $\boldsymbol{\varepsilon}_{Di}$ is the viscous strain in each term of the series. The solution of (22) at some time t, taking cognizance of the integral in (23), will require knowledge of the entire strain history to extract the PD solution. A computationally efficient way of implementing the viscoelastic constitutive model within the NOSBPD framework is to adopt an incrementalization algorithm. Similar approaches have been implemented for finite element methods (Simulia, 2011; Kaliske et al., 1997). Let the timeline be subdivided into discrete intervals such that $t^{n+1} = t^n + \Delta t$. Then the PD force density (22) at time t^{n+1} is give as:

$$\underline{\mathbf{T}}^{n+1} = \omega(|\boldsymbol{\xi}|)\left[3K\varepsilon_s^{n+1}\mathbb{I} + 2G_0\left(\boldsymbol{\varepsilon}_D^{n+1} - \sum_{i=1}^{n_G} \alpha_i \boldsymbol{\varepsilon}_{Di}^{n+1}\right)\right]\mathbf{K}^{-1}\boldsymbol{\xi} \tag{24}$$

where

$$\sigma_D = 2G_0\left(\boldsymbol{\varepsilon}_D^{n+1} - \sum_{i=1}^{n_G} \alpha_i \boldsymbol{\varepsilon}_{Di}^{n+1}\right) \tag{25}$$

represents the deviatoric stress at the end of the increment, such that the deviatoric stress increment is given by:

$$\Delta\boldsymbol{\sigma}_D(t) = 2G_0\left(\Delta\boldsymbol{\varepsilon}_D - \sum_{i=1}^{n_G} \alpha_i\left(\boldsymbol{\varepsilon}_{Di}^{n+1} - \boldsymbol{\varepsilon}_{Di}^{n}\right)\right) \tag{26}$$

The tangent modulus G^T is obtained by differentiating (26) with respect to the deviatoric strain increment $\Delta\boldsymbol{\varepsilon}_D$ which yields:

$$\mathrm{G}^T = \mathrm{G}_0\left[1 - \sum_{i=1}^{n_G} \alpha_i \frac{\tau_i}{\Delta t}\left(\frac{\Delta t}{\tau_i} + e^{-\Delta t/\tau_i} - 1\right)\right] \tag{27}$$

Let ε_D vary linearly with t such that:

$$\frac{d\boldsymbol{\varepsilon}_D}{dt} = \frac{\Delta\boldsymbol{\varepsilon}_D}{\Delta t} \tag{28}$$

Then, the expression for the viscous strain (23) can be written as

$$\boldsymbol{\varepsilon}_{Di}^{n+1} = \int_0^{t^n}\left(1 - e^{\left(\tau - t^{n+1}\right)/(\tau_i)}\right)\frac{d\boldsymbol{\varepsilon}_{Di}(\tau)}{d\tau} d\tau + \int_{t^n}^{t^{n+1}}\left(1 - e^{\left(\tau - t^{n+1}\right)/(\tau_i)}\right)\frac{d\boldsymbol{\varepsilon}_{Di}(\tau)}{d\tau} d\tau \tag{29}$$

By expressing $1 - e^{\left(\tau - t^{n+1}\right)/(\tau_i)} = 1 - e^{-\Delta t/\tau_i} + e^{-\Delta t/\tau_i}\left(1 - e^{(\tau - t^n)/(\tau_i)}\right)$ in (29), yields:

$$\boldsymbol{\varepsilon}_{Di}^{n+1} = \left(1 - e^{-\Delta t/\tau_i}\right)\int_0^{t^n}\frac{d\boldsymbol{\varepsilon}_D(\tau)}{d\tau} d\tau + e^{-\Delta t/\tau_i}\int_0^{t^n}\left(\left(1 - e^{(\tau - t^n)/(\tau_i)}\right)\right)\frac{d\boldsymbol{\varepsilon}_D(\tau)}{d\tau} d\tau + \frac{\Delta\boldsymbol{\varepsilon}_D}{\Delta t}\int_{t^n}^{t^{n+1}}\left(1 - e^{\left(\tau - t^{n+1}\right)/(\tau_i)}\right) d\tau \tag{30}$$

Utilizing the second of (23) and (30) yields an expression for the change in the $i-th$ viscous strain as:

$$
\begin{aligned}
\Delta\boldsymbol{\varepsilon}_{Di} &= \boldsymbol{\varepsilon}_{Di}^{n+1} - \boldsymbol{\varepsilon}_{Di}^{n} \\
&= \left(1 - e^{-\Delta t/\tau_i}\right) \int_0^{t^n} \frac{d\boldsymbol{\varepsilon}_D(\tau)}{d\tau} d\tau + e^{-\Delta t/\tau_i} \int_0^{t^n} \left(\left(1 - e^{(\tau - t^n)/(\tau_i)}\right)\right) \frac{d\boldsymbol{\varepsilon}_D(\tau)}{d\tau} d\tau + \frac{\Delta\boldsymbol{\varepsilon}_D}{\Delta t} \int_{t^n}^{t^{n+1}} \left(1 - e^{\left(\tau - t^{n+1}\right)/(\tau_i)}\right) d\tau - \int_0^{t^n} \left(1 - e^{-((t-\tau)/(\tau_i))}\right) \frac{d\boldsymbol{\varepsilon}_D}{d\tau}(\tau) d\tau \\
&= \left(1 - e^{-\Delta t/\tau_i}\right) \int_0^{t^n} \frac{d\varepsilon_D(\tau)}{d\tau} d\tau + \left(e^{-\Delta t/\tau_i} - 1\right) \int_0^{t^n} \left(\left(1 - e^{(\tau - t^n)/(\tau_i)}\right)\right) \frac{d\varepsilon_D(\tau)}{d\tau} d\tau + \frac{\Delta\varepsilon_D}{\Delta t} \int_{t^n}^{t^{n+1}} \left(1 - e^{\left(\tau - t^{n+1}\right)/(\tau_i)}\right) d\tau \\
&= \left(1 - e^{-\Delta t/\tau_i}\right)\varepsilon_D + \left(e^{-\Delta t/\tau_i} - 1\right)\varepsilon_{Di}^{n} + \frac{\Delta\varepsilon_D}{\Delta t}\left(\Delta t - \tau_i\left(1 - e^{-\Delta t/\tau_i}\right)\right) \\
&= \frac{\tau_i}{\Delta t}\left(\frac{\Delta t}{\tau_i} + e^{-\Delta t/\tau_i} - 1\right)\Delta\boldsymbol{\varepsilon}_D + \left(1 - e^{-\Delta t/\tau_i}\right)\left(\boldsymbol{\varepsilon}_D^{n} - \boldsymbol{\varepsilon}_{Di}^{n}\right)
\end{aligned} \tag{31}
$$

The change in viscous strain obtained from (31) is then used to update the current PD force density (23). If plane stress condition is assumed, then the stress in one of the coordinate direction is taken to be zero. Let the third component be the zero stress component. If the spherical strain ε_S is assumed to be known, then

$$\varepsilon_{33} = 3\varepsilon_S - \varepsilon_{11} - \varepsilon_{22} \tag{32}$$

Note also the definition of deviatoric strain $\boldsymbol{\varepsilon}_D = \boldsymbol{\varepsilon} - \varepsilon_S$, then

$$\varepsilon_{D_{33}} = 2\varepsilon_S - \varepsilon_{11} - \varepsilon_{22} \tag{33}$$

The out-of-plane deviatoric stress at the end of the increment (see (16)) is given as:

$$\boldsymbol{\sigma}_{D33}^{n+1}(t) = 2\mathrm{G}_0\left(\boldsymbol{\varepsilon}_{D33}^{n+1} - \sum_{i=1}^{n_G} \alpha_i \boldsymbol{\varepsilon}_{D33i}^{n+1}\right) \tag{34}$$

If we let $\boldsymbol{\varepsilon}_{D33}^{n+1} = \boldsymbol{\varepsilon}_{D33}^{n} + \Delta\boldsymbol{\varepsilon}_{D33}$, then (34) becomes

$$\boldsymbol{\sigma}_{D33}^{n+1}(t) = 2\mathrm{G}_0\left(\boldsymbol{\varepsilon}_{D33}^{n} + \Delta\boldsymbol{\varepsilon}_{D33} - \sum_{i=1}^{n_G} \alpha_i \left(\boldsymbol{\varepsilon}_{D33i}^{n} + \Delta\boldsymbol{\varepsilon}_{D33i}^{n}\right)\right) \tag{35}$$

Substituting (31) into (35) yields:

$$
\begin{aligned}
\boldsymbol{\sigma}_{D33}^{n+1}(t) &= 2\mathrm{G}^T \Delta\boldsymbol{\varepsilon}_{D33}^{n} + 2\mathrm{G}_0\left(1 - \sum_{i=1}^{n_G} \alpha_i \left(1 - e^{-\Delta t/\tau_i}\right)\right)\boldsymbol{\varepsilon}_{D33}^{n} \\
&\quad - 2\mathrm{G}_0 \sum_{i=1}^{n_G} \alpha_i e^{-\Delta t/\tau_i} \boldsymbol{\varepsilon}_{D33i}^{n}
\end{aligned} \tag{36}
$$

Now, standing on the assumption that bulk response is governed by elasticity, the volumetric stress at the end of the increment is given by:

$$\boldsymbol{\sigma}_S^{n+1}(t) = 3K\varepsilon_S^{n+1} \tag{37}$$

Note that the sum of deviatoric stress and spherical stress in the 3-direction is zero for plane stress condition. Therefore, the sum of (36) and (37) noting that $\varepsilon_S^{n+1} = \varepsilon_S^{n} + \Delta\varepsilon_S$ and writing $\overline{\boldsymbol{\sigma}}_{D33} = 2\mathrm{G}_0\left(1 - \sum_{i=1}^{n_G} \alpha_i \left(1 - e^{-\Delta t/\tau_i}\right)\right)\boldsymbol{\varepsilon}_{D33}^{n} - 2\mathrm{G}_0 \sum_{i=1}^{n_G} \alpha_i e^{-\Delta t/\tau_i} \boldsymbol{\varepsilon}_{D33i}^{n}$, yields:

$$3K\varepsilon_S^{n} + 3K\Delta\varepsilon_S + 2G^T \Delta\boldsymbol{\varepsilon}_{D33}^{n} + \overline{\boldsymbol{\sigma}}_{D33} = 0 \tag{38}$$

Note that from (33), the change in spherical strain in (38) can be written as $\Delta\varepsilon_{D_{33}} = 2\Delta\varepsilon_S - \Delta\varepsilon_{11} - \Delta\varepsilon_{22}$, so that with some rearrengement, (38) becomes:

$$\Delta\varepsilon_S = \frac{2G^T(\Delta\varepsilon_{11} - \Delta\varepsilon_{22}) - \overline{\boldsymbol{\sigma}}_{D33} - 3K\varepsilon_S^{n}}{\left(3K + 4G^T\right)} \tag{39}$$

Since ε_{11}^{n}, ε_{22}^{n} and ε_{33}^{n} and hence ε_S^{n} are known, (39) is used to update these quantities in the present time step t^{n+1}, from whence the PD force density vector $\mathbf{T}^{n+1}$ is obtained from (24).

4. Peridynamic computational homogenization theory

The PDCHT is a multiscale framework in which the homogenized or effective properties of a heterogeneous material are obtained based on information from the microscale by consideration of the macroscale deformation gradient. Based on the definition above, the PDCHT can be considered a first order nonlocal computational homogenization theory (Otero et al., 2018). The nonlocality is introduced into the framework through the NOSBPD.

The utilization of PDCHT to characterize complex material is driven by the goal of bridging the gap between the complex microscale interactions and the practical macroscale behaviour of the material. This is particularly relevant in the context of polycrystal ice, where a deeper understanding of how microscale features, as represented by grain orientation in this context, contributing to macroscopic behaviour can unlock critical insights for numerous applications, from infrastructure design to environmental monitoring. By achieving this, we not only gain insights into the fundamental behaviour of polycrystal ice but also pave the way for streamlined engineering analyses and designs that account for its unique characteristics.

4.1. Theoretical framework

Consider a microscopically heterogeneous material M. The objective of the PDCHT is to approximate the response of M with a constitutively equivalent microscopically homogeneous material $\overline{M}$. This approximation is based on the following two assumptions. The first assumption posits that if the constituent materials within M exhibit linear responses, then $\overline{M}$ will similarly exhibit a linear constitutive behaviour (Christensen, 1969; Hashin, 1965). Therefore, if the constitutive response of the constituent materials is assumed to be represented by the Hooke's law:

$$\sigma_{ij} = \mathrm{C}_{ijkl}\varepsilon_{kl} \tag{40}$$

then the constitutive response of $\overline{M}$ is given by:

$$\overline{\sigma}_{ij} = \overline{\mathrm{C}}_{ijkl}\overline{\varepsilon}_{kl} \tag{41}$$

where underscored variables in (41) denotes quantities associated with $\overline{M}$. The second assumption posits that the microscopically heterogeneous material is characterized by statistical homogeneity. This entails that M demonstrates consistent average behaviour across any randomly selected subregion of considerable size relative to the dimensions of individual microstructural elements or phases, such as grain size. Such a subregion is formally termed a Representative Volume Element (RVE).

Given that the implications of the first and second assumptions are granted, the determination of the response of $\overline{M}$ proceeds by establishing a relationship between micro-level stress and strain fields and their corresponding macro-level counterparts. This relationship is achieved through the application of the average stress and strain theorems (Galadima et al., 2023b). Consider a heterogeneous body $\mathfrak{B}$ occupying a domain $\overline{\Omega} = \Omega_s \bigcup \Omega c$, where Ω_s represents the solution domain and Ωc represents the boundary domain. Denoting the average stress and average strain over Ω_s as $\langle \boldsymbol{\sigma} \rangle$ and $\langle \boldsymbol{\varepsilon} \rangle$, respectively, the nonlocal average stress theorem posits that if $\mathfrak{B}$ attains static equilibrium under the action of a constant stress tensor $\overline{\boldsymbol{\sigma}}$ applied on the boundary domain Ωc, then the volume-averaged stress field within Ω_s equals $\overline{\boldsymbol{\sigma}}$ expressed as:

$$\langle \boldsymbol{\sigma} \rangle = \overline{\boldsymbol{\sigma}} \tag{42}$$

for (47) to satisfy (46) requires the integral in (47) to be zero, i.e.:

$$\frac{1}{V_{\Omega_s}} \int_{\Omega_c} \left((\sigma_{ik} - \overline{\sigma}_{ik}) \mathscr{S}^s_{\omega} x_k \left(u_i - x_j \overline{\varepsilon}_{ij} \right) \right) dV_{\Omega_c} = 0 \tag{48}$$

Satisfying (48) is accomplished by imposing appropriate boundary conditions. For example, consider applying homogeneous displacement field of the form:

$$\boldsymbol{u}(\boldsymbol{x}) = \overline{\boldsymbol{\varepsilon}} \boldsymbol{x} \tag{49}$$

where $\overline{\boldsymbol{\varepsilon}}$ is a prescribed strain tensor and $\boldsymbol{x}$ represents the coordinate of a material point. By substituting the displacement field from (49) into (48), it can be shown that this form satisfies the condition expressed in (48) as shown below:

$$\begin{aligned}
\frac{1}{V_{\Omega_s}} \int_{\Omega_c} \left((\sigma_{ik} - \sigma^*_{ik}) \mathscr{S}^s_{\omega} x_k \left(x_j \varepsilon^*_{ij} - x_j \varepsilon^*_{ij} \right) \right) dV_{\Omega_c} &= \frac{1}{V_{\Omega_s}} \int_{\Omega_c} \left((\sigma_{ik} - \sigma^*_{ik}) \mathscr{S}^s_{\omega} x_k \left(x_j - x_j \right) \varepsilon^*_{ij} \right) dV_{\Omega_c} \\
&= \frac{1}{V_{\Omega_s}} \int_{\Omega_c} \left((\sigma_{ik} - \sigma^*_{ik}) (\delta_{jk} - \delta_{jk}) \varepsilon^*_{ij} \right) dV_{\Omega_c} \\
&= \frac{1}{V_{\Omega_s}} \int_{\Omega_c} \left((\sigma_{ik} - \sigma^*_{ik}) (\varepsilon^*_{ik} - \varepsilon^*_{ik}) \right) dV_{\Omega_c} \\
&= 0
\end{aligned}$$

Furthermore, the nonlocal average strain theorem postulates that if $\mathfrak{B}$ experiences displacement on the boundary domain Ωc due to a constant strain tensor $\overline{\varepsilon}$, represented by $\boldsymbol{u}^0 = \overline{\boldsymbol{\varepsilon}} \boldsymbol{x}$ for all $\boldsymbol{x} \in \Omega c$, then it follows that:

$$\langle \boldsymbol{\varepsilon} \rangle = \overline{\boldsymbol{\varepsilon}} \tag{43}$$

where $\langle \boldsymbol{\sigma} \rangle$ and $\langle \boldsymbol{\varepsilon} \rangle$ are respectively given as:

$$\langle \sigma \rangle = \frac{1}{V_{\Omega_s}} \int_{\Omega_s} \boldsymbol{\sigma}(\mathbf{x}) dV_{\Omega_s} \tag{44}$$

and

$$\langle \boldsymbol{\varepsilon} \rangle = \frac{1}{V_{\Omega_s}} \int_{\Omega_s} \boldsymbol{\varepsilon}(\mathbf{x}) dV_{\Omega_s} \tag{45}$$

The implications from (42) and (43) is that once the stress or strain field is obtained as solution of a boundary volume constraint (BVC) problem over the RVE, then corresponding macro fields are easily obtained as volume averages of the micro fields. To enforce the constitutive equivalence between the microscopically heterogeneous material and the substitute microscopically homogeneous one as well as to ensure a unique solution to the BVC problem is obtained, appropriate boundary volume constraint must be applied to the RVE. These dual objectives are simultaneously achieved by satisfying the nonlocal macrohomogeneity condition:

$$\langle \sigma_{ij} \varepsilon_{ij} \rangle = \overline{\sigma}_{ij} \overline{\varepsilon}_{ij} \tag{46}$$

One way of satisfying (46) is through the lemma (Galadima et al., 2023b):

$$\langle \sigma_{ij} \varepsilon_{ij} \rangle - \overline{\sigma}_{ij} \overline{\varepsilon}_{ij} = \frac{1}{V_{\Omega_s}} \int_{\Omega_c} \left((\sigma_{ik} - \overline{\sigma}_{ik}) \mathscr{S}^s_{\omega} x_k \left(u_i - x_j \overline{\varepsilon}_{ij} \right) \right) dV_{\Omega_c} \tag{47}$$

In this context, the notation S^s_{ω} represents a symmetric gradient operator weighted by ω, with the superscript S indicating its symmetric nature. For an in-depth understanding of the nonlocal gradient operator and the general elements of nonlocal vector calculus, refer to (Galadima et al., 2023b; Du et al., 2013; Gunzburger et al., 2010). Observe that in order

4.2. Implementation of the PDCHT

The numerical implementation of the PDCHT in this study follows a displacement-based homogenization procedure. This approach involves subjecting the RVE to prescribed displacements at its boundaries. The objective is to determine the displacement field, followed by the strain field, and ultimately the stress field within the RVE by utilizing the peridynamic field equation (3).

Since the goal is to obtain the effective material tensor, it is necessary to apply as many boundary conditions as the size of the matrix representing the material tensor. In two dimensions, the material tensor is represented by a 3 × 3 matrix. Therefore, three different iterations of (49) are required. A straightforward way to accomplish this is by successively applying the following strain tensors:

$$\overline{\boldsymbol{\varepsilon}}^{(1)} = \begin{bmatrix} c & 0 \\ 0 & 0 \end{bmatrix}, \overline{\boldsymbol{\varepsilon}}^{(2)} = \begin{bmatrix} 0 & 0 \\ 0 & c \end{bmatrix}, \overline{\boldsymbol{\varepsilon}}^{(3)} = \begin{bmatrix} 0 & c/2 \\ c/2 & 0 \end{bmatrix} \tag{50}$$

where c is the magnitude of the prescribed strain tensor. The resultant displacements for each iteration are given by:

$$\boldsymbol{u}_i^{(1)} = \begin{Bmatrix} c\alpha_i \\ 0 \end{Bmatrix}, \boldsymbol{u}_i^{(2)} = \begin{Bmatrix} 0 \\ c\beta_i \end{Bmatrix}, \boldsymbol{u}_i^{(3)} = \begin{Bmatrix} c\alpha_i \\ c\beta_i \end{Bmatrix} \tag{51}$$

where α_i and β_i are the components of the coordinates of the material point. Once the local stress field within the RVE is resolved, the average stress $\langle \boldsymbol{\sigma} \rangle$ is computed using (44) (specific to the displacement-based method). This average stress is then utilized to recover the effective material tensor which in turn yields the effective modulus E and Poisson's ratio ν. This approach ensures that the effective properties derived from the computational homogenization procedure are reflective of the local stress and strain distributions within the RVE, thus facilitating a comprehensive characterization of the polycrystalline ice's behaviour under different loading conditions.

5. Computational homogenization of S2 ice

In this validation study, the objective is to assess the accuracy of PDCHT by solving several specimens of polycrystalline S2 ice. All

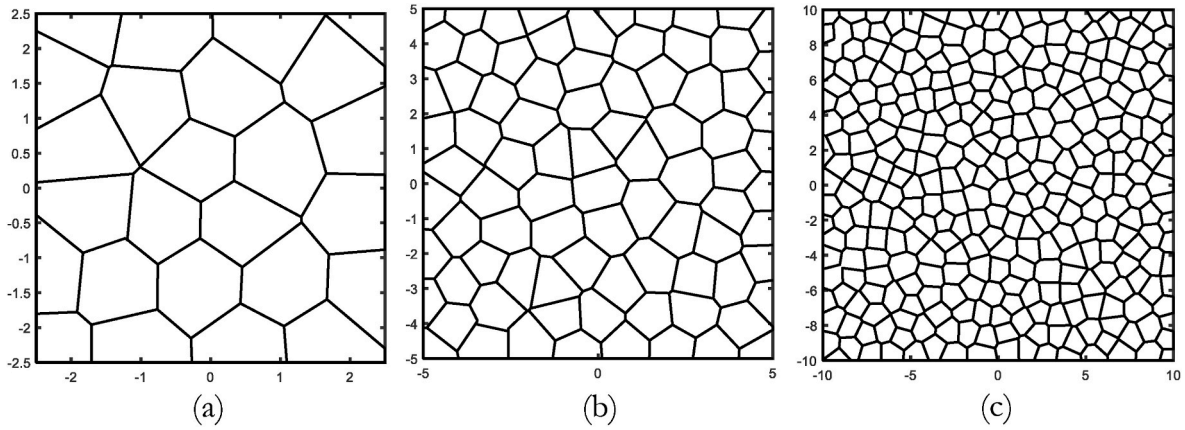

Fig. 2. Typical grain geometries for specimen size of (a) 5 × 5 mm^2, (b) 10 × 10 mm^2, and (c) 20 × 20 mm^2.

Table 1
Sample size and grain characteristics for samples corresponding to (Elvin, 1996).

Specimen Size mm^2	Number of grains	Average grain area mm^2
5 × 5	25	1.0
7.5 × 7.5	50	1.1
10 × 10	85	1.2
12.5 × 12.5	125	1.3
15 × 15	180	1.3
17.5 × 17.5	235	1.3
20 × 20	305	1.3

Table 2
Sample size and grain characteristics for samples corresponding to (Li et al., 2023).

Specimen size mm^2	Number of grains	Average grain area mm^2
50 × 50	49	51.02
64 × 64	81	50.57
78 × 78	121	50.28
85 × 85	144	50.17
92 × 92	169	50.08
99 × 99	196	50.01
106 × 106	225	49.94
113 × 113	256	49.88
121 × 121	289	50.66

specimens are of square geometry to ensure consistency and comparability in the study. To achieve a comprehensive validation, the PDCHT results will be compared with data from two previously conducted studies, namely, Elvis (Elvin, 1996) and Li et al. (2023). To replicate the results obtained in (Elvin, 1996), seven specimen sizes have been considered, including 5 × 5 mm^2, 7.5 × 7.5 mm^2, 10 × 10 mm^2, 12.5 × 12.5 mm^2, 15 × 15 mm^2, 17.5 × 17.5 mm^2, and 20 × 20 mm^2. Likewise, for the replication of results obtained in (Li et al., 2023), nine specimen sizes of 50 × 50 mm^2, 64 × 64 mm^2, 78 × 78 mm^2, 85 × 85 mm^2, 92 × 92 mm^2, 99 × 99 mm^2, 106 × 106 mm^2, 113 × 113 mm^2, and 121 × 121 mm^2 have been investigated.

For each specimen, a prescribed strain of $c = 1$ (refer to equation (50)) is applied to evaluate the mechanical response. Fig. 2 (a, b, and c) show representative specimens with grain geometries corresponding to specimen sizes of 5 × 5 mm^2, 10 × 10 mm^2, and 20 × 20 mm^2, respectively. These specimens contain 25, 85, and 305 grains, respectively.

Since the cross-section of columnar ice typically exhibits a polygonal grain shape (Sinha, 1989), Voronoi polygons are employed to represent the grain geometry in this study. It is worth noting that this choice aligns with the approach used in (Elvin, 1996) as well as (Li et al., 2023). The process of obtaining these Voronoi polygons begins with defining a set of nucleation points or seeds. The number of seeds corresponds to the number of grains in the specimen under consideration. To ensure the representation of ice grains with approximately equal areas, these nucleation points are selected randomly but with a constraint such that they must be spaced a minimum distance apart. This constraint is applied to ensure uniformity in the ice grain sizes (Sinha, 1989). The size, number of grains and the average grain size for the two cases investigated are given in Tables 1 and 2. Bar graphs showing the distribution of grain sizes for specimen of sizes 20 × 20 and 121 × 121 are presented in Figs. 3(a) and 4(a), respectively. In Fig. 3(a), it is evident that a significant proportion of the grains possess sizes close to the average value of 1.3 mm^2, which aligns with the average grain size reported in (Elvin, 1996). Similarly, Fig. 4(a) shows that the majority of the grains exhibit sizes close to the average value of 50.66 mm^2, consistent with the average grain size reported in (Li et al., 2023).

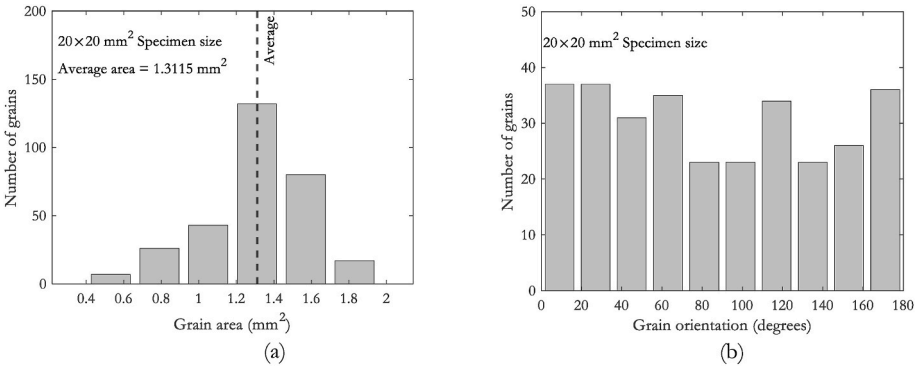

Fig. 3. A bar graph for a 20 × 20 (mm) RVE showing; (a) Grain area; (b) Grain orientation.

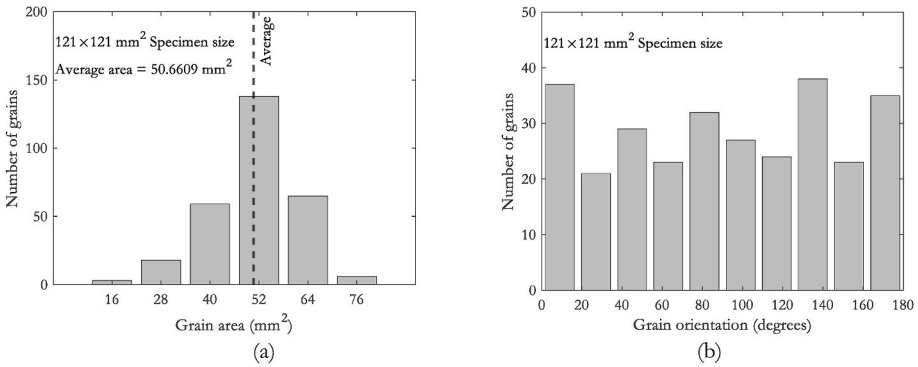

Fig. 4. A bar graph for a 121 × 121 (mm) RVE showing; (a) Grain area; (b) Grain orientation.

Following the definition of grain geometry, each grain within the specimen is assigned a random grain orientation. This orientation is selected from a range spanning from 0 to 180°. A histogram illustrating the distribution of these uniformly chosen grain orientations for specimens of size 20 × 20 and 121 × 121 are presented in Figs. 3(b) and 4(b) respectively.

5.1. Elastic material properties

The 3D dynamic elastic stiffness tensor of the ice crystal at a temperature of −16 °C, as derived from (Elvin, 1996) is given as:

$$\begin{bmatrix} 15.010 & 5.765 & 5.765 & 0 & 0 & 0 \\ & 13.929 & 7.082 & 0 & 0 & 0 \\ & & 13.929 & 0 & 0 & 0 \\ & & & 3.4235 & 0 & 0 \\ & Sym & & & 3.014 & 0 \\ & & & & & 3.014 \end{bmatrix} \text{GPa} \tag{52}$$

For numerical convenience, plane stress condition is assumed to apply. Thus from (12) and (13), the equivalent two-dimensional elastic modulus is given as:

$$\begin{bmatrix} 12.624 & 2.832 & 0 \\ 2.832 & 10.328 & 0 \\ 0 & 0 & 3.014 \end{bmatrix} \text{GPa} \tag{53}$$

The c-axis of the ice crystal has an angular inclination of 45° relative to the global x_1 axis.

5.2. Result of simulations

To determine the homogenized properties of polycrystalline ice samples, thirty simulations were conducted for each sample configuration. The first set of simulations, corresponding to the study in (Elvin, 1996), used consistent grain geometries with randomly generated grain orientations for each iteration. The second set, corresponding to (Li et al., 2023), randomized both the grain geometries and orientations for each simulation.

5.2.1. Effective properties analysis

Tables 3 and 4 analysis (First set of Specimens):

- Young's Modulus (E_1 and E_2): The results demonstrate that as the number of grains increases, the homogenized Young's modulus values converge more rapidly. For instance, with 25 grains (5 mm × 5 mm), the percentage difference in E_1 is 7.03%, decreasing significantly to 1.93% for 305 grains (20 mm × 20 mm). This trend indicates that a higher grain count results in more consistent mechanical properties and reduced variability in Young's modulus. Similarly, E_2 shows a convergence trend with decreasing percentage differences from 7.23% to 2.15% across the grain range.
- Poisson's ratios (ν_{12} and ν_{21}): The Poisson's ratios also show a decrease in percentage difference with increasing grain count. For ν_{12}, the percentage difference decreases from 14.11% (25 grains) to 3.89% (305 grains), while ν_{21} reduces from 13.41% to 3.11%. This trend demonstrates that an increased number of grains leads to more isotropic behaviour, as noted in (Elvin, 1996).

Tables 5 and 6 Analysis (Second Set of Specimens):

- Young's Modulus (E_1 and E_2): For larger specimens, such as those with 49 grains (50 mm × 50 mm), the percentage difference in E1 is 6.16%, decreasing to 2.58% for 289 grains (121 mm × 121 mm). This trend further supports the findings from the first set, emphasizing the critical role of grain count in achieving isotropic mechanical behaviour
- Poisson's ratios (ν_{12} and ν_{21}): The percentage differences for ν_{12} and ν_{21} also decrease as the grain count increases, with ν_{12} reducing from 14.37% to 4.70% and ν_{21} from 11.47% to 3.82%. This corroborates the trend observed in the first set, highlighting the role of grain distribution in influencing isotropy.

5.2.2. Results discussion

The results from Tables 3–6 illustrate a clear trend: the homogenized elastic properties, converge more rapidly with an increasing number of grains. This trend is consistent across both specimen sets and aligns with

Table 3
Homogenized properties E_1 and ν_{12} for sample sizes consistent with (Elvin, 1996).

Spacemen Size (mm²)	E_1 (MPa)				ν_{12}			
	Min	Ave	Max	% Diff	Min	Ave	Max	% Diff
5 × 5	9194.03	9534.49	9840.01	7.03	0.305	0.326	0.348	14.108
7.5 × 7.5	9215.38	9543.97	9814.96	6.51	0.308	0.327	0.340	10.252
10 × 10	9358.24	9601.06	9792.60	4.64	0.314	0.327	0.341	8.759
12.5 × 12.5	9383.02	9602.02	9774.07	4.17	0.315	0.326	0.342	8.556
15 × 15	9456.73	9613.09	9758.92	3.20	0.318	0.328	0.339	6.513
17.5 × 17.5	9426.32	9606.33	9747.10	3.40	0.317	0.326	0.334	5.592
20 × 20	9516.675	9627.72	9700.29	1.93	0.319	0.325	0.331	3.889

Table 4
Homogenized properties E_2 and ν_{21} for sample sizes consistent with (Elvin, 1996).

Spacemen Size (mm^2)	E_2 (MPa)				ν_{21}			
	Min	Ave	Max	% Diff	Min	Ave	Max	% Diff
5 × 5	9252.66	9612.51	9921.29	7.23	0.307	0.329	0.348	13.405
7.5 × 7.5	9359.53	9597.90	9948.32	6.29	0.316	0.329	0.347	9.655
10 × 10	9331.63	9567.49	9764.82	4.64	0.313	0.326	0.342	9.380
12.5 × 12.5	9366.13	9598.02	9788.66	4.51	0.316	0.326	0.342	8.036
15 × 15	9379.52	9561.91	9720.43	3.63	0.317	0.326	0.337	6.508
17.5 × 17.5	9475.32	9605.46	9750.29	2.90	0.316	0.326	0.337	6.700
20 × 20	9510.72	9618.29	9715.14	2.15	0.320	0.325	0.330	3.113

Table 5
Homogenized properties E_1 and ν_{12} for sample sizes consistent with (Li et al., 2023).

Spacemen Size (mm^2)	E_1 (MPa)				ν_{12}			
	Min	Ave	Max	% Diff	Min	Ave	Max	% Diff
50 × 50	9353.71	9593.72	9930.24	6.16	0.31	0.32	0.35	14.37
64 × 64	9384.44	9583.64	9911.93	5.62	0.31	0.33	0.34	10.56
78 × 78	9467.87	9602.12	9748.80	2.97	0.32	0.33	0.34	6.90
85 × 85	9415.93	9621.55	9810.82	4.19	0.31	0.33	0.33	6.71
92 × 92	9429.94	9612.64	9779.62	3.71	0.32	0.33	0.34	7.71
99 × 99	9445.83	9599.95	9737.25	3.09	0.32	0.33	0.33	5.51
106 × 106	9481.66	9594.98	9735.15	2.67	0.32	0.33	0.34	5.66
113 × 113	9459.62	9619.22	9764.43	3.22	0.32	0.33	0.34	5.01
121 × 121	9481.56	9615.89	9725.96	2.58	0.32	0.33	0.33	4.70

Table 6
Homogenized properties E_2 and ν_{21} for sample sizes consistent with (Li et al., 2023).

Spacemen Size (mm^2)	E_2 (MPa)				ν_{21}			
	Min	Ave	Max	% Diff	Min	Ave	Max	% Diff
50 × 50	9168.23	9619.05	9917.15	8.17	0.31	0.33	0.34	11.47
64 × 64	9368.54	9582.90	9972.46	6.45	0.31	0.33	0.34	8.76
78 × 78	9402.86	9579.52	9815.92	4.39	0.32	0.33	0.34	5.43
85 × 85	9475.28	9584.15	9838.80	3.84	0.31	0.33	0.34	7.49
92 × 92	9353.22	9589.78	9740.23	4.14	0.32	0.33	0.34	6.93
99 × 99	9477.56	9596.74	9737.90	2.75	0.32	0.33	0.34	5.66
106 × 106	9455.93	9600.99	9730.35	2.90	0.32	0.33	0.33	4.91
113 × 113	9435.94	9577.84	9699.88	2.80	0.32	0.33	0.33	5.34
121 × 121	9479.63	9611.70	9733.56	2.68	0.32	0.33	0.33	3.82

findings from (Elvin, 1996) and (Li et al., 2023).

- Convergence of Young's Moduli: The relatively faster convergence of Young's moduli compared to Poisson's ratios suggests that elastic stiffness stabilizes more quickly as the grain count increases. This implies that the mechanical stiffness of polycrystalline ice becomes less sensitive to variations in grain orientation and distribution at higher grain counts, leading to more predictable and uniform behaviour.
- Role of Grain Count: The decreasing percentage differences with increasing grain count underscore the critical role of microstructural elements in determining the macroscopic mechanical response of polycrystalline ice. As the number of grains increases, the effects of individual grain orientations diminish, resulting in a more isotropic material behaviour. This finding is particularly relevant for applications requiring precise predictions of mechanical properties in polycrystalline ice.
- Validation Against Previous Studies: The consistency of these results with prior studies further validates the use of PDCHT as an effective tool for modelling the mechanical behaviour of polycrystalline ice. The ability of PDCHT to capture the impact of grain count and orientation distribution on isotropy and mechanical properties demonstrates its robustness and applicability in ice mechanics.

5.3. Effective elastic properties and the Voigt-Reuss bounds

The Voigt (V) and Reuss (R) formulas are commonly employed to estimate the upper and lower bounds of the effective elastic properties of heterogeneous materials. The V-R bounds for the elastic properties of S2 ice in the plane of isotropy at -16°C were computed in (Nanthikesan et al., 1994) as follows:

$$\begin{aligned} 9.726 \geq \overline{\mathrm{E}} \geq 9.431 \\ 0.320 \leq \overline{\nu} \leq 0.334 \end{aligned} \tag{54}$$

where $\overline{\mathrm{E}}$ and $\overline{\nu}$ are the homogenized Young's modulus and Poisson's ratio respectively. Figs. 5 and 6 show plots of the homogenized elastic constants $\overline{\mathrm{E}}$ and $\overline{\nu}$ obtained from simulations corresponding to (Elvin, 1996) and (Li et al., 2023), respectively. In these figures, the V-R bounds are also included. These graphical representations offer a convenient means of analysing how the number of grains in an ice sample affects the computed effective elastic constants.

Figs. 5(a) and 6(a) display the band of the homogenized Young's modulus $\overline{E}$, while Figs. 5(b) and 6(b) show the band of effective Poisson's ratio $\overline{\nu}$ derived from the computations. Each band results from running the simulation 30 times for a specified number of grains. As expected, increasing the number of grains in a sample has the effect of narrowing the band of the effective properties. In both simulations, samples containing more than 225 grains exhibit narrower bands of effective elastic

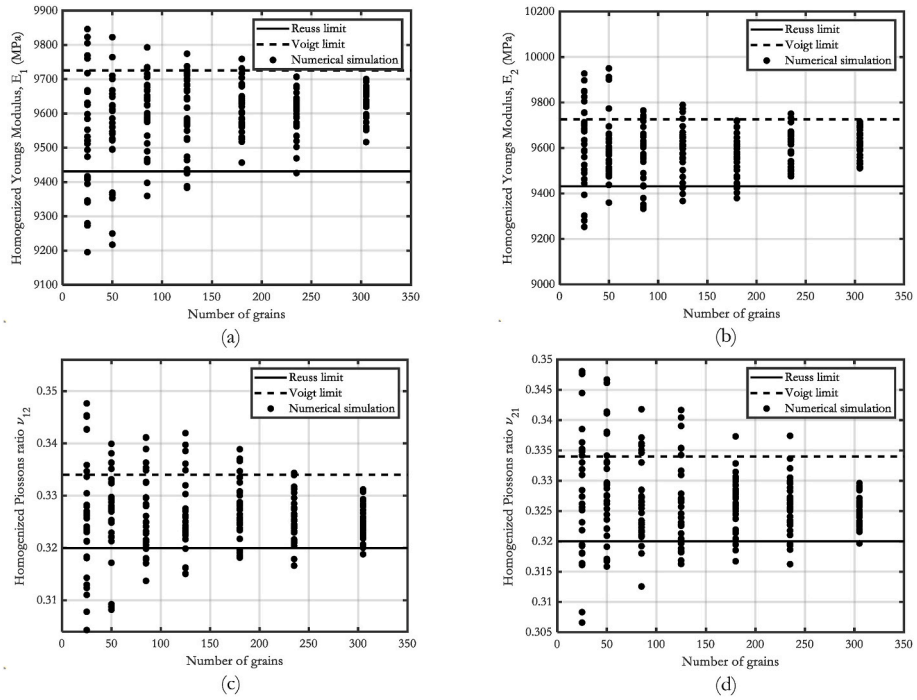

Fig. 5. Homogenized elastic properties consistent with (Elvin, 1996): (a) Young's modulus E_1, (b) Young's modulus E_2, (c) Poisson's ratio ν_{12}, (d) Poisson's ratio ν_{21}.

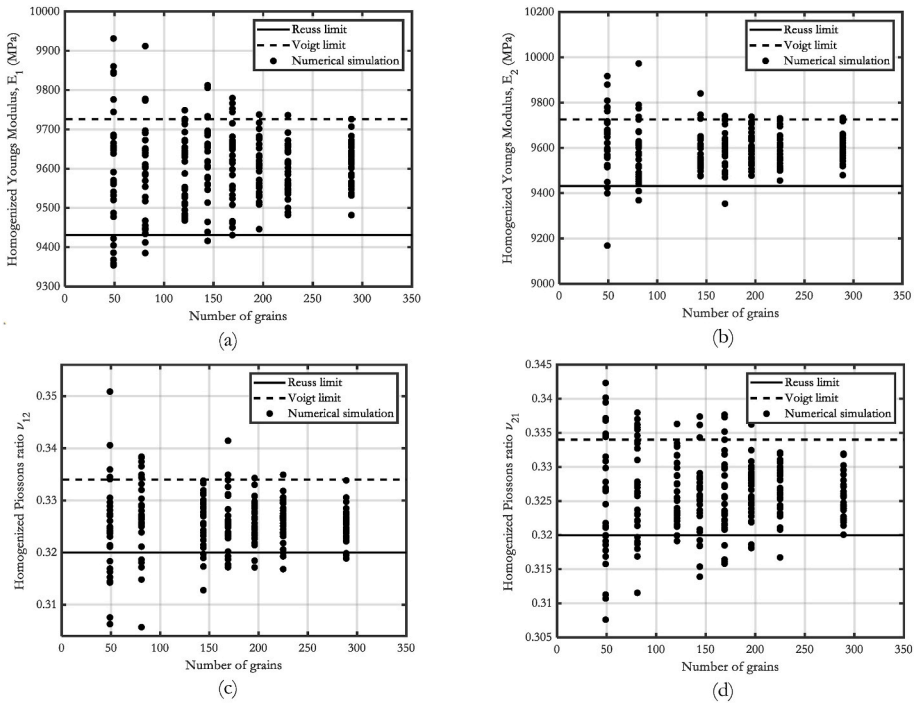

Fig. 6. Homogenized elastic properties consistent with (Li et al., 2023): (a) Young's modulus E_1, (b) Young's modulus E_2, (c) Poisson's ratio ν_{12}, (d) Poisson's ratio ν_{21}.

constants compared to the limiting V-R bounds. Consequently, it can be inferred that a sample of S2 ice with more than 225 grains can serve as a representative area for polycrystalline ice, aligning with the findings in (Duddu et al., 2013) and (Silling, 2000).

5.4. Degree of anisotropy as a function of number of grains in a sample

Further analysis of how the number of grains affect the effective elastic properties of S2 ice is conducted by measuring the degree of anisotropy with increasing grain number in the ice samples. Various methods exist to quantify the elastic anisotropy of materials, with one of the earliest proposed approaches presented by Zener and Siegel (Zener et al., 1949). This method, initially proposed for cubic crystals, assesses the degree of anisotropy using a scalar parameter known as the Zener anisotropy index, $A_z = 2C_{33} / (C_{11} - C_{12})$, where C_{ij} represents components of the elastic stiffness tensor.

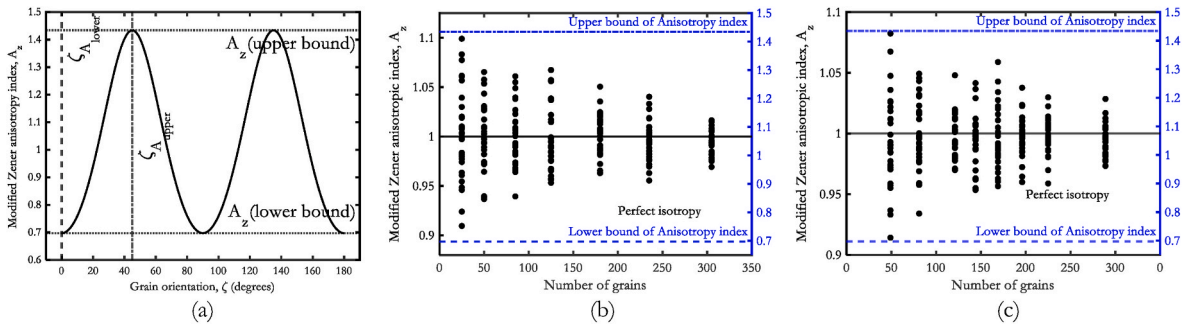

Fig. 7. Modified Zener anisotropy index.

However, for the purposes of this study, we will employ the modified Zener anisotropy index proposed in (Li et al., 2023). This modified index is formulated as follows:

$$A_z = \frac{4C_{33}}{C_{11} + C_{22} - C_{12} - C_{21}} \tag{55}$$

Fig. 7(a) presents the anisotropic index for a single grain, covering grain orientations in the range of $0 \leq \zeta \leq 180$. From Fig. 7(a), the extremum values of the modified Zener anisotropy index, A_z' correspond to grain orientations $\zeta = 0^o$ and $\zeta = 45^o$. These values serve as the upper and lower bounds for the degree of anisotropy exhibited by the S2 ice. These are subsequently compared with the anisotropy index computed from the simulations. Fig. 7(b) shows the anisotropy index resulting from computations corresponding to (Elvin, 1996), while Fig. 7(c) illustrates the anisotropy index derived from computations corresponding to (Li et al., 2023). Due to the considerable disparity in magnitude between the anisotropy index computed from simulation and the bounding values, we have chosen to present them on the same plot using different axes. This approach ensures a clearer and more informative representation of our data. As evident in Fig. 7(b)–(c), the more grains contained in a sample, the more the effective response of the sample tends towards isotropic behaviour.

5.5. Comparison with experimental results

As noted in section 5.3, samples with number of grains greater than 230 provide effective elastic properties that mostly lie within a band that is narrower than the V-R bounds. It is therefore expected that the effective elastic properties computed from any sample with number of grains more than 230 should be at per with experimental data. In this respect, the effective elastic constants computed from two samples with sizes 17.5×17.5 mm^2 and 113×113 mm^2 with 235 and 256 number of grains respectively will be compared with experimental data from (Gold, 1958) and (Sinha, 1978). The equivalent elastic stiffness tensors of the 17.5×17.5 mm^2 and 113×113 mm^2 samples, which are taken as the averages of the respective homogenized elastic stiffness tensors, are respectively given as:

$$\begin{bmatrix} 10.747 & 3.502 & 0.001 \\ 3.499 & 10.746 & -0.007 \\ 0.002 & -0.005 & 3.608 \end{bmatrix} \text{GPa, and} \quad \begin{bmatrix} 10.766 & 3.507 & 0.004 \\ 3.505 & 10.720 & 0.008 \\ 0.002 & 0.006 & 3.616 \end{bmatrix} \text{GPa} \tag{56}$$

From (56), the equivalent elastic constants for the two samples at temperature of -16^oC are computed, and the results are presented in Table 7. From Table 7, the effective Young's modulus for S2 columnar ice is predicted to lie in the range $9.606 \leq E \leq 9.607$ and $9.578 \leq E \leq 9.620$, while the corresponding effective Poisson's ratio is predicted to be $\nu = 0.326$ and to lie between $0.326 \leq \nu \leq 0.327$ for the 17.5×17.5 and 113×113 samples respectively. Note that the equivalent Young's moduli and Poisson's ratios computed above are at -16^oC. However, the data from referenced experimental studies are reported at different temperatures. To facilitate for comparisons with experimental data, the equivalent Young's modulus computed from the simulation of the two samples are corrected for temperatures of -5^oC and -40^oC using (11) and the results are also presented in Table 7.

The Young's modulus obtained from the experimental work in (Gold, 1958) at temperature of -5^oC as reported in (Elvin, 1996) lie in the range 8.95 GPa and 9.94Gpa, while the Poisson's ratio lies in the range 0.31 and 0.365. In (Sinha, 1978), the result of experimental observation conducted in the temperature range of -40^oC and -45^oC was reported to lie in the range of 9.1 GPa and 9.8 GPa. A comparison of these experimental results with results from the numerical simulation presented in Table 7 shows good agreement. This agreement with experimental data highlights the validity and accuracy of the numerical simulations across a spectrum of temperatures, enhancing the robustness of our findings.

6. Study of viscoelastic ice response using NOSBPD

In this section, the viscoelastic constitutive model presented in Section 2 will be integrated into the Non-Ordinary State-Based Peridynamics (NOSBPD) framework. The aim is to extend the application of NOSBPD to capture the time-dependent, viscoelastic response of ice, which is known to exhibit viscoelastic properties under various loading conditions. This section will start by describing the computational implementation of the integral viscoelastic model (equation (18)) and how the constitutive model is integrated into the NOSBPD framework. This will be followed by a benchmark simulation to validate the NOSBPD framework against Finite Element simulation of the same problem. These simulations will highlight the effectiveness of NOSBPD in modelling the viscoelastic behaviour of ice.

6.1. Viscoelastic response of ice sample subjected to tensile stress

In this subsection, the benchmark problem, simulation setup, and parameters are described for analysing the viscoelastic response of an ice

Table 7
Equivalent elastic constants at -16^oC.

sample	$T = -16^o$C				$T = -5^o$C		$T = -40^o$C	
	ν_{12}	ν_{21}	E_{11}	E_{22}	E_{11}	E_{22}	E_{11}	E_{22}
17.5×17.5 mm^2	0.326	0.326	9.607	9.606	9.460	9.460	9.927	9.926
113×113 mm^2	0.327	0.326	9.620	9.578	9.473	9.432	9.940	9.897

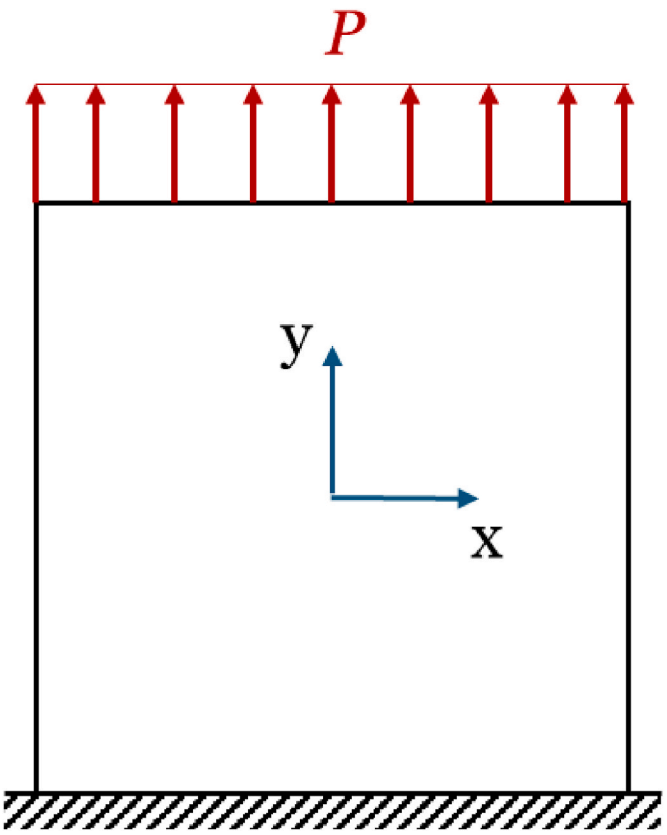

Fig. 8. Simulation setup showing ice sample subjected to tensile load for viscoelastic analysis.

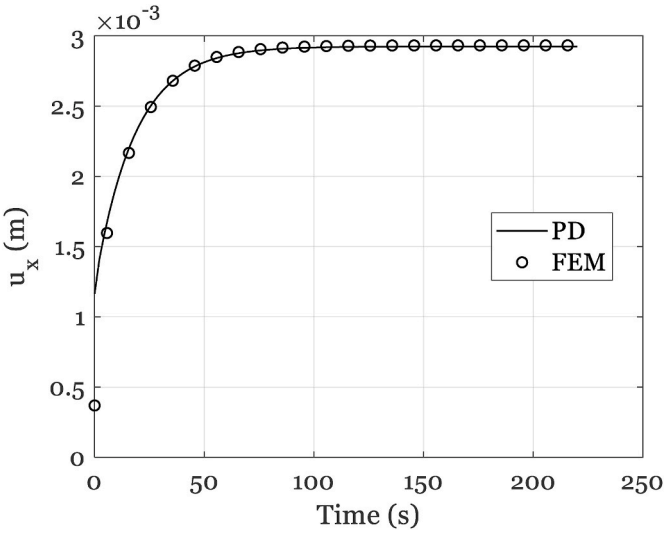

Fig. 9. Comparison of the evolution of displacement in the x-direction in a viscoelastic ice sample subjected to tensile stress.

sample subjected to tensile stress. The sample is a square ice sample with unit dimensions. The left edge of the ice sample is fixed, while a tensile load $P = 0.45$ MPa is applied to the right edge.

For the numerical implementation, the solution domain is discretized into a grid where the spacing between points along the x and y directions are equal, denoted as dx and dy respectively, with $dx = dy$. The horizon δ is chosen such that $\delta = 3dx$.

The simulation setup, illustrating the boundary conditions and loading configuration, is shown in Fig. 8. Under the assumption of bulk

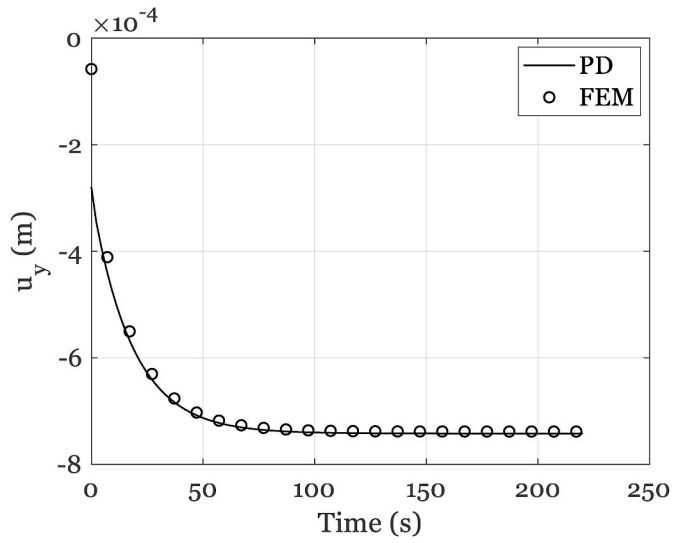

Fig. 10. Comparison of the evolution of displacement in the y-direction in a viscoelastic ice sample subjected to tensile stress.

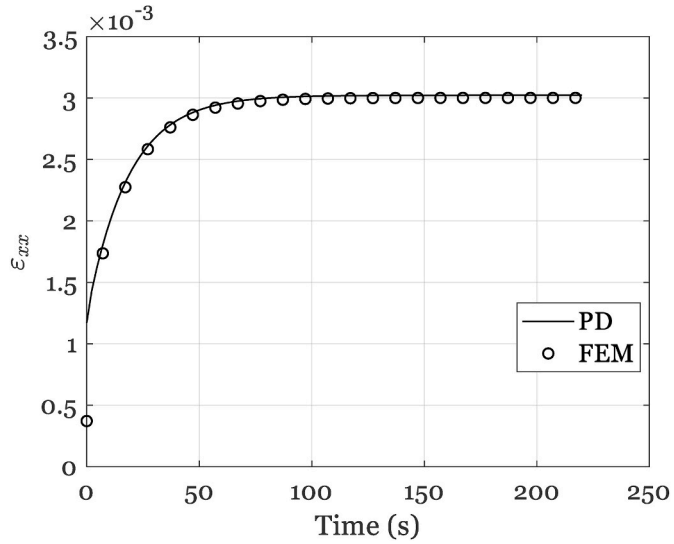

Fig. 11. Comparison of the evolution of strain response.

elastic response and viscoelastic response being governed by shear, the bulk and shear relaxation modulus G (t) of the ice as derived from (Swamidas et al., 1978) are:

$$\mathrm{K} = 5244\mathrm{MPa}, \mathrm{G}(t) = \mathrm{G}_{\infty} + \sum_{i=1}^{2} \mathrm{G}_i e^{-t/\tau_1} \tag{57}$$

where $\mathrm{G}_{\infty} = 51.2$ MPa, $\mathrm{G}_1 = 86.9$ MPa, $\mathrm{G}_2 = 333$ MPa, $\tau_1 = 400$ Minutes, and $\tau_2 = 4.2$ Minutes.

To present the results obtained using the NOSBPD, a material point Q located at coordinate x = 0.5 and y = 0.5 was selected, and its displacement was tracked over time. The x-displacement of point Q is presented in Fig. 9, while the y-displacement is presented in Fig. 10. For comparison, a finite element model (FEM) of the same problem was simulated in ANSYS Mechanical, and the results are presented alongside.

Fig. 9 presents the x-displacement of point Q over time. The displacement curve obtained from the NOSBPD simulation shows a gradual increase with time, indicating the viscoelastic nature of the material. The FEM simulation results are plotted alongside for comparison. The x-displacement curve from the FEM simulation closely

follows the trend observed in the NOSBPD results, demonstrating a good agreement between the two methods. This alignment suggests that the NOSBPD model accurately captures the viscoelastic response of the ice sample under tensile loading.

Similarly, Fig. 10 shows the y-displacement of point Q as a function of time. The y-displacement curve from the NOSBPD simulation also exhibits a viscoelastic behaviour. The FEM simulation results are also presented alongside for comparison. The y-displacement curve from the FEM simulation closely matches the NOSBPD results, reinforcing the accuracy and robustness of the NOSBPD model in predicting the viscoelastic behaviour of the ice sample.

To further validate the NOSBPD model, a typical plot of strain versus time is presented in Fig. 11, with the corresponding results from the FEM simulation included for comparison. The strain-time curve from the NOSBPD simulation reflects the expected viscoelastic response, characterized by an initial rapid increase in strain, followed by a gradual approach to an asymptotic value. The FEM simulation results exhibit a similar trend, closely matching the NOSBPD curve.

The comparison of displacement and strain results between the NOSBPD and FEM simulations reveals a high degree of correlation, indicating that the NOSBPD framework effectively captures the viscoelastic behaviour of ice under tensile loading. The good agreement between the two methods validates the NOSBPD model as a reliable tool for simulating the time-dependent response of ice. This validation is crucial for the continued development and application of PD in the field of ice mechanics, providing a robust alternative to traditional FEM simulations.

7. Conclusion

This study has successfully explored the elastic and viscoelastic behaviour of ice using the Non-Ordinary State-Based Peridynamic (NOSBPD) framework, significantly contributing to the expanding discourse on peridynamics in ice mechanics. The key findings from both the elastic and viscoelastic studies are as follows:

Utilizing the PDCHT within the NOSBPD framework, this study identified the critical threshold of grain count necessary to induce an effectively isotropic response in polycrystalline S2 ice. The results were consistent with previous studies, further validating the robustness of the NOSBPD and PDCHT frameworks. Additionally, the study extended the application of NOSBPD to capture the viscoelastic response of ice. By integrating a viscoelastic constitutive model within the NOSBPD framework, the simulation results showed good agreement with FEM simulations conducted in ANSYS Mechanical. This demonstrates the capability of NOSBPD to accurately model time-dependent, viscoelastic behaviours of ice under tensile loading.

This research advances the understanding and application of NOSBPD in ice mechanics by demonstrating its effectiveness and robustness in capturing both elastic and viscoelastic responses. The validation of PDCHT in homogenizing polycrystalline ice also underscores its potential for practical applications in ice mechanics.

Future studies could extend the NOSBPD and PDCHT frameworks to investigate the response of ice under more complex loading conditions, such as cyclic or impact loading, to further validate its applicability in dynamic scenarios. Incorporating more detailed material properties, such as temperature-dependent behaviours, ageing and anisotropic characteristics, could enhance the accuracy of NOSBPD simulations in capturing more complex mechanics of ice.

CRediT authorship contribution statement

Yakubu Kasimu Galadima: Writing – original draft, Software, Methodology, Conceptualization. **Erkan Oterkus:** Writing – review & editing, Supervision, Methodology, Conceptualization. **Selda Oterkus:** Writing – review & editing, Supervision, Methodology, Conceptualization.

Declaration of competing interest

The authors declare that they have no known competing financial interests or personal relationships that could have appeared to influence the work reported in this paper.

References

Candaş, A., Oterkus, E., İmrak, C.E., 2020. Dynamic crack propagation and its interaction with micro-cracks in an impact problem. J. Eng. Mater. Technol. 143 (1).

Christensen, R.M., 1969. Viscoelastic properties of heterogeneous media. J. Mech. Phys. Solid. 17 (1), 23–41.

Du, Q., et al., 2013. A nonlocal vector calculus, nonlocal volume-constrained problems, and nonlocal balance laws. Math. Model Methods Appl. Sci. 23 (3), 493–540.

Duddu, R., Waisman, H., 2013. A nonlocal continuum damage mechanics approach to simulation of creep fracture in ice sheets. Comput. Mech. 51 (6), 961–974.

Elvin, A.A., 1996. Number of grains required to homogenize elastic properties of polycrystalline ice. Mech. Mater. 22 (1), 51–64.

Galadima, Y.K., et al., 2022. Peridynamic computational homogenization theory for materials with evolving microstructure and damage. Eng. Comput.

Galadima, Y.K., et al., 2023a. Modelling of viscoelastic materials using non-ordinary state-based peridynamics. Eng. Comput.

Galadima, Y.K., et al., 2023b. A computational homogenization framework for non-ordinary state-based peridynamics. Eng. Comput. 39 (1), 461–487.

Gammon, P.H., et al., 1983. Elastic constants of artificial and natural ice samples by brillouin spectroscopy. J. Glaciol. 29 (103), 433–460.

Gold, L.W., 1958. Some observations on the dependence of strain on stress for ice. Can. J. Phys. 36 (10), 1265–1275.

Gold, L.W., 1977. Engineering properties of fresh-water ice. J. Glaciol. 19 (81), 197–212.

Gu, X., Zhang, Q., Madenci, E., 2019. Non-ordinary state-based peridynamic simulation of elastoplastic deformation and dynamic cracking of polycrystal. Eng. Fract. Mech. 218, 106568.

Gunzburger, M., Lehoucq, R.B., 2010. A nonlocal vector calculus with application to nonlocal boundary value problems. Multiscale Model. Simul. 8 (5), 1581–1598.

Hashin, Z., 1965. Viscoelastic behavior of heterogeneous media. J. Appl. Mech. 32 (3), 630–636.

Kaliske, M., Rothert, H., 1997. Formulation and implementation of three-dimensional viscoelasticity at small and finite strains. Comput. Mech. 19 (3), 228–239.

Li, J., et al., 2023. Peridynamic modeling of polycrystalline S2 ice and its applications. Eng. Fract. Mech. 277, 108941.

Liu, M., Wang, Q., Lu, W., 2017. Peridynamic simulation of brittle-ice crushed by a vertical structure. Int. J. Nav. Archit. Ocean Eng. 9 (2), 209–218.

Liu, R., Yan, J., Li, S., 2020. Modeling and simulation of ice–water interactions by coupling peridynamics with updated Lagrangian particle hydrodynamics. Computat. Particle Mech. 7 (2), 241–255.

Londono, J.G., Berger-Vergiat, L., Waisman, H., 2016. A Prony-series type viscoelastic solid coupled with a continuum damage law for polar ice modeling. Mech. Mater. 98, 81–97.

Lu, W., et al., 2020. Peridynamic modelling of fracture in polycrystalline ice. J. Mech. 36 (2), 223–234.

Nanthikesan, S., Shyam Sunder, S., 1994. Anisotropic elasticity of polycrystalline ice Ih. Cold Reg. Sci. Technol. 22 (2), 149–169.

Otero, F., Oller, S., Martinez, X., 2018. Multiscale computational homogenization: review and proposal of a new enhanced-first-order method. Arch. Comput. Methods Eng. 25 (2), 479–505.

Shi, C., et al., 2017. A nonlinear viscoelastic iceberg material model and its numerical validation. Proc. IME M J. Eng. Marit. Environ. 231 (2), 675–689.

Silling, S.A., 2000. Reformulation of elasticity theory for discontinuities and long-range forces. J. Mech. Phys. Solid. 48 (1), 175–209.

Silling, S.A., et al., 2007. Peridynamic states and constitutive modeling. J. Elasticity 88 (2), 151–184.

Simulia, 2011. *Abaqus* Theory Manual.

Sinha, N.K., 1978. Rheology of columnar-grained ice. Exp. Mech. 18 (12), 464–470.

Sinha, N.K., 1989. Experiments on anisotropic and rate-sensitive strain ratio and modulus of columnar-grained ice. J. Offshore Mech. Arctic Eng. 111 (4), 354–360.

Song, Y., Yu, H., Kang, Z., 2018. Numerical study on ice fragmentation by impact based on non-ordinary state-based peridynamics. J. Micromech. Molecul. Phys. 4 (1), 1850006.

Song, Y., et al., 2019. Peridynamic modeling and simulation of ice craters by impact. Computer Modeling in Engineering \& Sciences 121 (2), 465–492.

Song, Y., Li, S., Li, Y., 2023. Peridynamic modeling and simulation of thermo-mechanical fracture in inhomogeneous ice. Engineering with Computers 39 (1), 575–606.

Swamidas, A., El-Tahan, H.W.M., Reddy, D., 1978. Viscoelastic Finite-Element Analysis of Floating Ice Islands. Faculty of Engineering and Applied Science, MUN.

Zener, C.M., Siegel, S., 1949. Elasticity and anelasticity of metals. The Journal of Physical and Colloid Chemistry 53 (9), 1468, 1468.